RESEARCH ARTICLE

Key Points:
- Estimate permeability in low-resolution μ-CT data using correlations with computed rock characteristics
- Significant predictors include computed formation factor, open pore fraction, and open pore size
- Computed formation factor uses image gray scales, thereby capturing pore length-scale information

Correspondence to:
P. W. S. K. Botha,
pwsk.botha@gmail.com

Mapping permeability in low-resolution micro-CT images: A multiscale statistical approach

Pieter W. S. K. Botha[1] and Adrian P. Sheppard[1]

[1]Department of Applied Mathematics, Research School of Physical Sciences and Engineering, The Australian National University, Canberra, Australian Capital Territory, Australia

Abstract We investigate the possibility of predicting permeability in low-resolution X-ray microcomputed tomography (μCT). Lower-resolution whole core images give greater sample coverage and are therefore more representative of heterogeneous systems; however, the lower resolution causes connecting pore throats to be represented by intermediate gray scale values and limits information on pore system geometry, rendering such images inadequate for direct permeability simulation. We present an imaging and computation workflow aimed at predicting absolute permeability for sample volumes that are too large to allow direct computation. The workflow involves computing permeability from high-resolution μCT images, along with a series of rock characteristics (notably open pore fraction, pore size, and formation factor) from spatially registered low-resolution images. Multiple linear regression models correlating permeability to rock characteristics provide a means of predicting and mapping permeability variations in larger scale low-resolution images. Results show excellent agreement between permeability predictions made from 16 and 64 μm/voxel images of 25 mm diameter 80 mm tall core samples of heterogeneous sandstone for which 5 μm/voxel resolution is required to compute permeability directly. The statistical model used at the lowest resolution of 64 μm/voxel (similar to typical whole core image resolutions) includes open pore fraction and formation factor as predictor characteristics. Although binarized images at this resolution do not completely capture the pore system, we infer that these characteristics implicitly contain information about the critical fluid flow pathways. Three-dimensional permeability mapping in larger-scale lower resolution images by means of statistical predictions provides input data for subsequent permeability upscaling and the computation of effective permeability at the core scale.

1. Introduction

With the availability of three-dimensional imaging techniques such as micro X-ray computed tomography (μ-CT), it is becoming common practice to determine fluid flow properties in reservoir and aquifer rocks through direct image-based simulation [*Bell*, 2001; *Turner et al.*, 2004; *Riepe et al.*, 2011; *Blunt et al.*, 2013]. In computed tomography imaging, field of view and image resolution are directly related through the number of voxels in each dimension in the reconstructed tomogram [*Sakellariou et al.*, 2004]. Lower resolution images, such as those of whole core samples, provide greater sample coverage and capture more sample heterogeneity, but do not adequately represent the pore structure and cannot be used for direct permeability computation. On the other hand, images with higher resolution permitting direct computation of fluid flow properties have correspondingly smaller fields of view. These small images, though high in resolution, only cover a representative volume for the most homogenous rocks and are very different in scale from core plugs used in conventional experiments. High-resolution μ-CT imaging can generally be achieved for sample sizes ranging from 5 to 25 mm in diameter; however, sample size limits are very much a function of the imaging system in question. For samples greater than 25 mm diameter, one would start considering the use of whole core or medical CT scanners, keeping in mind that medical CT images of whole core often provide little information about petrophysical properties. Classifying an image as high or low-resolution depends on how the image resolution compares to the scales of sample textures. Two core plug samples of 10 mm diameter, one with fine and one with coarse textures, could be imaged at the same absolute resolution (say 8 μm/voxel), and the image of the fine texture sample considered to be low-resolution and that of the course texture sample to be high-resolution, based on the extent to which the rock texture is captured within each image.
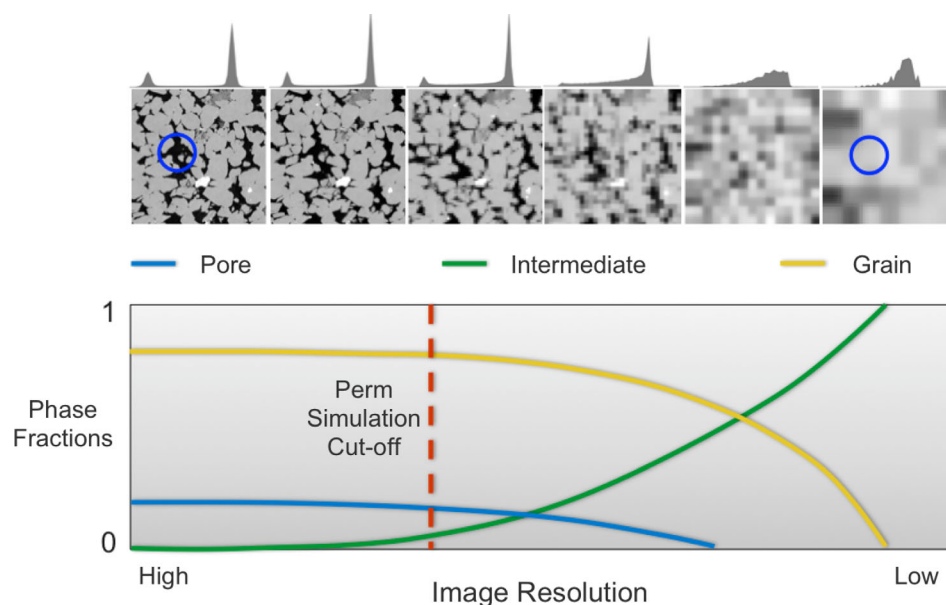
Figure 1. The effect of image resolution on phase identification. High-resolution images resolve pore space geometry with high fidelity while at low-resolution pores are represented partially or completely by intermediate gray scale values.

Several authors have shown that absolute and relative permeability, both key petrophysical parameters, are strongly dependent on pore space geometry [*Doyen*, 1988; *Fredrich et al.*, 1993; *Pape et al.*, 1999], therefore, reliable simulation results can only be achieved from images that accurately represent all major flow paths within the rock's pore space. This work focuses on developing a workflow to predict and map absolute permeability variations over the large fields of view obtainable from lower-resolution tomographic images, such as images of whole core samples. The approach is based on statistical correlations between low-resolution characteristics and high-resolution computed permeability. Such a permeability map can ultimately be used as input for permeability upscaling at the whole core scale and beyond. Multiphase transport properties will be the subject of future work.

1.1. Image Resolution and Property Computation

Figure 1 is a qualitative diagram showing the theoretical effect of image resolution on phase proportions and the ability to compute absolute permeability. Consider a two-component system comprising one solid phase (grains) and one air phase (pores). With modern 3-D scanning systems achieving micron and nanometer-scale imaging resolution [*Metz et al.*, 2009; *Varslot et al.*, 2010; *Cnudde and Boone*, 2013] the two components are well differentiated and a histogram of gray scale intensities shows only two peaks, one gray scale value for each component. As image resolution decreases (e.g., for imaging larger fields of view), an increasing fraction of the voxels lie on the surfaces between grain and pores and thus appear as intermediate gray-scale values, because the volume sampled by those voxels includes both grain and pore (the "partial volume effect"). With a further decrease in image resolution, the proportion of intermediate gray scale voxels increases and the proportions of voxels representing the original two components decrease. At some pore-size–dependent resolution, the interconnections within the pore space (i.e., pore throats) start to be represented by intermediate gray scale values and direct transport modeling becomes impossible. Extracting information from images in this regime, where transport pathways cease to be fully resolved, is the focus of this work.

At even lower resolution, the spatial averaging associated with each voxel covers such a large volume that all geometric information is lost. It is normally considered that medical CT scanning, with a typical resolution of around 500 μm/voxel, falls into this last category. With a complete absence of geometric information, CT scans of whole core are not used to estimate permeability, and it seems unlikely that worthwhile information for predicting transport properties could be extracted.

Archie [1942] described the formation resistivity factor (F) of porous material in terms of its porosity (ϕ) and the cementation exponent (m) with the equation $F = \phi^{-m}$. *Berg* [2012] and *Zhang and Knackstedt* [1995] evaluate electrical conductance and highlight the importance of pore geometry and flow path tortuosity. *Arns et al.* [2001b] investigate the effects of image resolution and associated discretization (segmentation) errors, such as poor representation of pore geometry, on the numerical computation of electrical conductivity. For a single sample represented by a range of image resolutions, they observed systematic overestimation of formation factor with decreasing image resolution.

Permeability simulations in this study are based on the Lattice-Boltzmann method for solving the Navier-Stokes flow equation, where the fluid is represented as generalized particles [*Arns et al.*, 2004] and placed under a pressure gradient by a body force throughout the volume [*Ferréol and Rothman*, 1995], or by constant-pressure boundary conditions. *Martys et al.* [1999] were among the first to identify the need for sufficient imaging resolution in their experiments with Fontainebleau sandstone. Generally permeability simulations only return useful results if the image resolution is sufficiently high to represent flow pathways in the pore system with at least four open voxels, i.e., the voxel size needs to be 4 times smaller than the diameter of the smallest pore throats that lie on percolating flow paths. This is dictated by the simulation algorithm that applies no-slip conditions at the solid-fluid interfaces: with four voxels spanning, a pore throat only the inner two voxels allow significant fluid flow. In lower-resolution images, the pore throats are depicted by intermediate gray scale voxels (rather than open pore voxels) and consequently do not allow flow during simulation: the simulated permeability will therefore be zero regardless of the actual permeability. *Apourvari and Arns* [2014] assess the effect of subresolution porosity on permeability and use a Lattice Boltzmann method modified with the Brinkman approach [*Brinkman*, 1949] that includes regions of subresolution porosity in the permeability computation by applying Darcy's law to such regions. This approach suffers the shortcoming that one must estimate the permeability of the subresolution porosity, often without knowledge of the pore space geometry.

In studying the effect of image resolution on permeability simulation, *Peng et al.* [2014] found that two μ-CT images of Berea Sandstone with resolutions of 1.85 and 5.92 μm/voxel return nearly identical permeability, indicating that the latter is high enough resolution to capture the main flow paths for that rock, and that the smaller pores need not always be resolved. *Zhang et al.* [2000] investigated the scale dependency of the so-called representative element volume (REV), a range of physical sample volumes for which a measured quantity such as permeability does not change. Their results show that the REV for a Brent Triassic Sandstone sample is considerably larger than that of a sample of crushed glass beads, because of the increased degree of heterogeneity of the sandstone. In the context of image resolution and field of view, and depending on the sample heterogeneity, it is clear that for any given sample, volumes that fall in the range of an REV may not always have sufficient resolution to allow permeability simulation.

1.2. Permeability Prediction

Predicting the permeability of aquifer and reservoir rocks based on laboratory measurements of rock characteristics has long been a topic of interest. The Kozeny-Carman equation [*Carman*, 1956; *Aubertin and Chapuis*, 2003] is a well-known method of estimating permeability for porous material and forms the basis for subsequent work by [*Van Baaren*, 1979; *Paterson*, 1983; *Walsh and Brace*, 1984]. Their method is based on the theory of fluid flow through a set of capillary tubes where permeability is described as a function that includes the pore space specific surface area, the void ratio, and a constant taking into account channel shape and tortuosity. *Swanson* [1981] was among the first to investigate the use of parameters derived from a capillary pressure curve to estimate permeability, suggesting that the point defining the maximum mercury saturation to pressure ratio defines the effective connecting porosity. *Katz and Thompson* [1986] continued the use of the capillary pressure curves but instead use it to derive a pore system length scale they refer to as the characteristic length (l_c). They propose an expression that relates permeability to a universal constant (C), the characteristic length and the electrical conductivity (σ/σ_o) (equation (1)).

$$k = C l_c^2 \left(\frac{\sigma}{\sigma_0}\right) = C l_c^2 \frac{1}{F} = C l_c^2 \tau \tag{1}$$

The characteristic length is determined from the capillary pressure inflection point on the mercury intrusion curve, which is suggested to correspond with the establishment of a connected mercury cluster. In the

absence of grain surface conductivity, the electrical conductivity is the inverse of the formation factor $(1/F)$, which captures the connectedness of the pore system and can be expressed in terms of tortuosity (τ) [*Clennell*, 1997]. *Berg* [2014] provides an excellent summary of works related to permeability estimation in the context of characteristic length, tortuosity, and porosity.

In the context of detailed 3-D imaging, the characteristic length can be given a precise geometric definition as the diameter of the largest sphere that can pass through the pore system. *Arns et al.* [2005] use parameters computed from μ-CT images to predict permeability using empirical methods, including Kozeny-Carman and Katz-Thompson, and correlate the results with Lattice Boltzmann simulated permeability. They conclude that for resolutions where it is possible to compute, the characteristic length provides the best measure of length scale to predict permeability.

More recently, *Dehghan Khalili et al.* [2013] focus on carbonate reservoir rock and investigate the use of porosity-permeability relationships derived from μ-CT images to estimate permeability in larger-scale lower resolution μ-CT images.

Benavente et al. [2015] propose permeability prediction in sandstones and carbonates through a series of statistical models based on the relationships between laboratory measurements of permeability and capillary imbibition, porosity, and pore structure. Their recommended models include the capillary absorption coefficient and connected porosity, but not mean pore radius, which does not improve the statistical fit of their regression models.

1.3. Contribution of This Work

This paper explores the fundamentals of predicting the spatial variations in absolute permeability of heterogeneous sandstone from high field of view tomographic images whose resolution is not sufficient to allow direct permeability computation. The unique contribution is the development of a new workflow that combines existing analytical techniques to predict the spatial distribution of absolute permeability throughout the large field of view of low-resolution μ-CT images, such as images of whole core, where permeability cannot be computed directly by numerical methods. This workflow predicts the permeability of many small homogeneous regions within low-resolution images, providing information that is unavailable from bulk laboratory techniques, by statistically correlating the permeability computed from regions in high-resolution images with rock characteristics determined from the same regions in low-resolution images. Segmentation of lower resolution images (binarizing the image) typically eliminates much of the gray scale information related to pore geometry. In addition to macroscale quantities such as porosity, this work explores the use of a segmentation technique that preserves gray scale information and allows the computation of characteristics that incorporate image gray scales. Such characteristics should have the potential to correlate well with geometry-dependent properties like permeability.

Absolute permeability is computed directly on high-resolution images by numerical solution of the Navier-Stokes equations using the Lattice Boltzmann method, while characteristics such as open pore fraction, pore size, and formation factor are calculated from low-resolution images and used as predictor variables of permeability. To better understand their predictive ability, each characteristic is correlated with permeability in a series of ordinary least squares (OLS) models. The most promising characteristics are then combined and correlated with permeability in multiple linear models.

The essential steps in the proposed workflow are:

1. Acquire a low-resolution (LR) 3-D image of a core sample that spans a relatively large volume of the rock (in this work: 25 mm diam. × 80 mm long).
2. Acquire a high-resolution (HR) image of one or more subsamples of the core, and compute directly the permeability on homogeneous regions within each image. In total, the subsamples should span the bulk of the rock texture variability.
3. Digitally align the low and high-resolution images to locate the overlap region.
4. Calibration: determine statistical correlations between permeability (from HR image) and rock characteristics (from the aligned overlap region of the LR image).
5. Prediction: calculate rock characteristics for the LR image of the whole core plug from step 1 and predict permeability using the statistical correlations from step 4.

Optionally, the workflow may include more than two levels of imaging to span a larger range of length scales. In the context of reservoir-scale modeling and simulation, the predicted permeabilities obtained
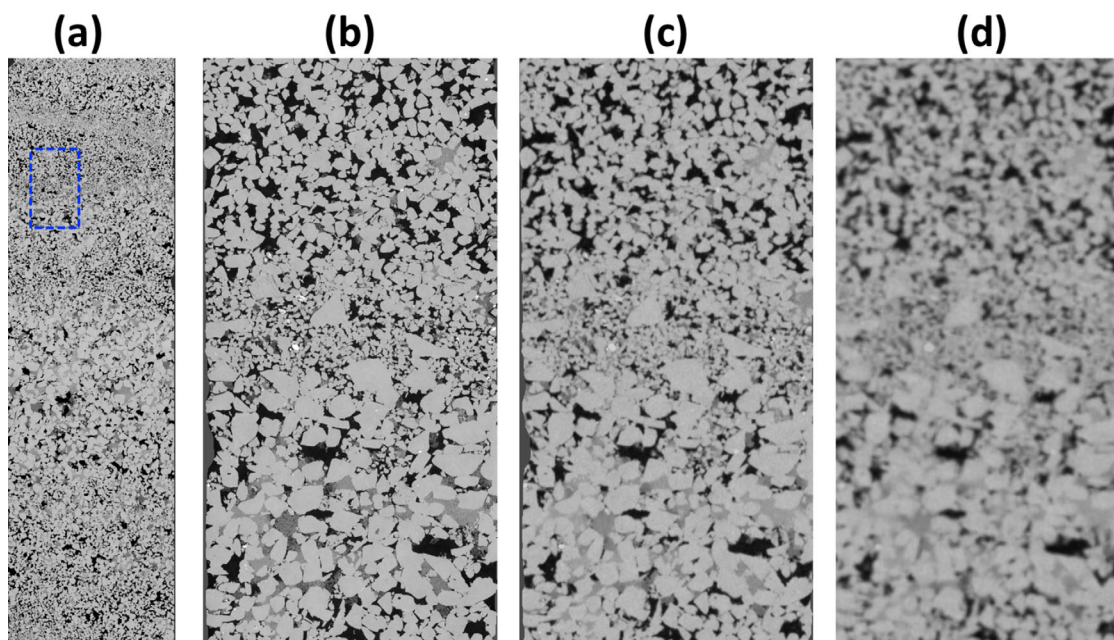
Figure 2. (a) The 25 mm core plug imaged at 16 μm/voxel; (b) the 5 μm/voxel image of the 8 mm subplug; and (c and d respectively) the overlap regions from the 16 μm/voxel and 64 μm/voxel images. The blue square indicates the approximate location of the 8 mm subplug.

from this workflow for individual rock units can ultimately be used to compute effective permeability at the core scale by means of Darcy simulation techniques [*Kløv et al.*, 2003].

2. Methods

2.1. Sampling and Imaging

This paper reports on two core plugs (sample 1 and sample 2) from the Precipice Sandstone in the Surat Basin, Australia, which can be considered a good example of relatively clean siliciclastic aquifer rock. It is highly porous and permeable, with generally less than 10% clay, and limited silica redistribution. Deposited by a low sinuosity braided river system [*Martin*, 1977], the Precipice Sandstone contains fine to coarse-grained laminations ranging from one millimeter to several centimeters in thickness. In this work, we apply the previously described permeability prediction workflow to two 25 mm diameter 80 mm tall core plugs. In the main body of the paper, we discuss the development of the workflow in the context of the results from sample 1, and then report on the main results from sample 2 in section 4. The 25 mm core plugs were first imaged rapidly as part of a bundle with other cores to produce image (1) a low-resolution image at ~64 μm/voxel, after which image (2) an intermediate resolution image at ~16 μm/voxel was acquired through a high-fidelity scan of the core plugs in isolation. Finally, image (3) a high-resolution image at ~5 μm/voxel was acquired through physical coring and imaging of a 8mm diameter 15 mm long subplug from the original core plug of sample 1. The high-resolution image for sample 2 was collected using a "region of interest scan" (see section 4). The three images for each of the core plugs are aligned to one another using a distributed-memory parallel cross-scale 3-D image registration algorithm [*Latham et al.*, 2008a,b]. In addition to the high-fidelity imaging of significant sample heterogeneity across multiple scales, this imaging program enables the study of cross-scale correlations because of precise voxel to voxel registration of the images to each other. The overlap regions between the images provide information at all three resolutions; therefore, the statistical calibration step is restricted to the domain of the high-resolution image. Figure 2 shows the difference in resolution between the images and the approximate location of the subplug for sample 1. The location for collecting the subplug was selected for both practical and analytical considerations. Based on visual assessment, the subplug location was selected to provide the best sampling across the range of relatively fine, medium, and coarse textures. The coarsest lamination in the subplug is poorly cemented and necessitates a 8 mm diameter subplug to avoid sample damage that may occur during coring to a smaller diameter. Furthermore, the 8 mm diameter makes it possible to collect reliable data
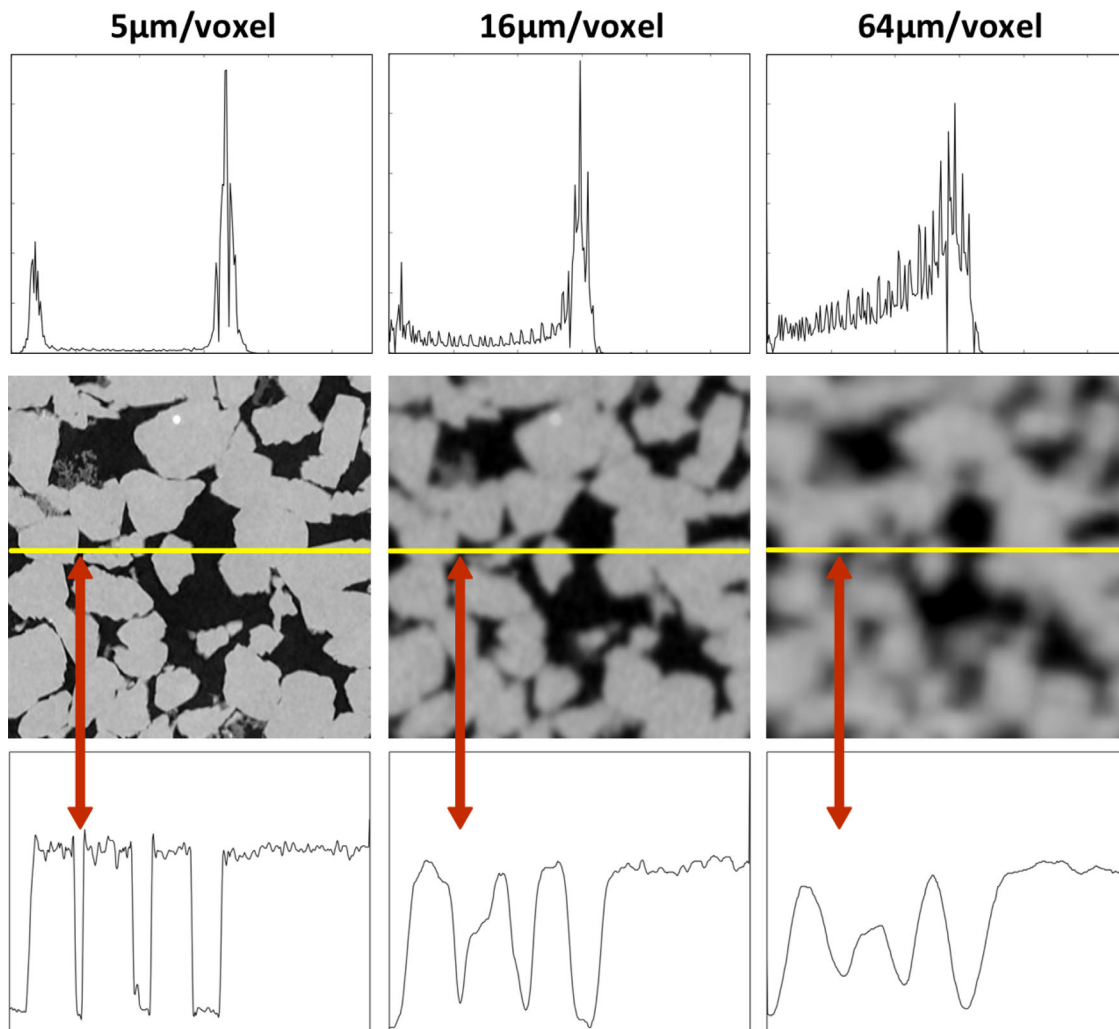
Figure 3. Close-up regions taken from the three different resolution images. Each image has an accompanying gray scale histogram above and intensity profile below (indicated by the yellow lines). Note how the change in resolution is reflected in the smoothing of the intensity profile. The red arrows indicate a narrow pore space, which is resolved in the high-resolution image, but represented by intermediate gray scale values in the low-resolution image.

on a larger volume of the coarsest lamination. Given the configuration of the μ-CT imaging equipment, the 8 mm diameter subplug can be imaged with a maximum resolution of ∼5 μm/voxel, which is sufficient to accurately represent the pore system in all three rock textures. As we discuss in section 3.4, it is worth noting that the analytical results may be affected if the subplug is chosen in such a way that it does not represent the range of rock textures present in the larger-scale sample, or if it is too large for accurate imaging of the finest textures in the heterogeneous pore system. Since the images were not constructed through a digital downsampling procedure, they all contain real imaging artifacts such as noise and blur.

Figure 3 shows 2-D slices, gray scale histograms and intensity profiles of select regions of the registered low, intermediate, and high-resolution images. The reduction in image resolution causes significant smoothing of the intensity profile and the inability to capture smaller features is evident. Furthermore, the intensity histogram of the 64 μm/voxel image shows an overall increase of intermediate gray scale values due to spatial averaging (blurring), which results in many regions of the pore space, most notably the pore throats, being completely occupied by intermediate gray scale values.

The resolution of images 1 and 3 differ by a factor of 13, corresponding to a reduction in volumetric sampling density of over 2000, i.e., image 1 can cover a volume 2000 times larger than that of image 3, given an image of the same number of voxels.
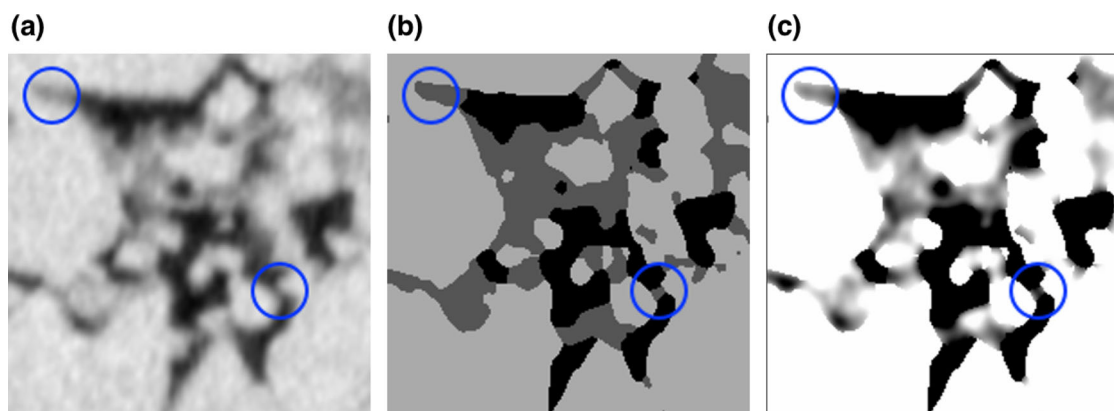
Figure 4. (a) A 2-dimensional slice from a 16 μm/voxel gray scale tomogram, (b) the equivalent segmented (binarized) image showing the loss of gray scale and geometric information associated with segmentation, and (c) the inclusion of gray scale information with the microporosity segmentation method for intermediate intensity voxels.

2.2. Image Segmentation

Conventionally the 65,535 gray levels in the 16 bit gray scale images are partitioned into a smaller number of phases, with each phase representing a different class of material. Typically the segmented phases are: pore, intermediate phase (clays), and solid phase (framework minerals). However, segmentation generally causes a loss of geometric information contained in the image gray scales. Figures 4a and 4b show how pore throats may be closed during segmentation and how corners and crevasses of pores are not always accurately represented by a segmented image, especially at low-resolution. Here we make use of a two-stage segmentation method. First, using the converging active contour method [*Sheppard et al.*, 2004], where the gray scale values are divided into three main phases; and second, a "soft" thresholding segmentation procedure (microporosity segmentation) allocates 100 gray levels to intermediate intensity voxels to build a porosity map, which includes subresolution pores within the intermediate phase (Figure 4c). Each voxel in the intermediate phase is assigned a value based on a linear interpolation between a minimum and maximum attenuation value corresponding to 100% pore and 100% grain, respectively [*Sok et al.*, 2009]. This process assumes that the intensity of each intermediate-phase voxel in the image is linearly related to the porous fraction of that voxel. This is a tolerable assumption for the very simple mineralogy of the Precipice Sandstone studied here; however, for more complex rock types, it would be necessary to perform more reliable porosity mapping using a method such as the multiimage wet/dry imaging workflow described in *Sheppard et al.* [2014].

2.3. Image Unitization

Figure 5 shows that the sample used for this study contains significant heterogeneity with fine, medium, and coarse-grained bands. To improve the probability of identifying correlations between rock properties and absolute permeability, a unitization procedure was developed to identify internally homogeneous zones, or units, for individual characterization. We should emphasize that this procedure is not intended for rock classification. It serves to isolate internally homogenous zones within the image for individual analysis with minimal overlap. The method makes use of the gradient of the grain-size profile, calculated from covering radius transform (CRT) data [*Hazlett*, 1995], and open pore fraction profile to identify points of maximum change along the length of the core sample. These points of maximum change are considered potential boundaries between units. The method iteratively compares and merges adjacent units based on a user-adjustable threshold [*Botha et al.*, 2014]. The result is a series of units in which the grain size and pore fraction of each unit are distinct from its neighbors'. For the overlap region between all three images, the unitization procedure identified three units based on grain size. The pore fraction profile has too little variation to warrant subdivision into units.

To increase the number of data points for the statistical correlations, each unit is subdivided into a series of approximately cubic subvolumes. Absolute permeability and predictor rock characteristics are computed for each subvolume, and, therefore, each unit separately. The top and bottom boundaries for the subvolumes for each unit are chosen to match those from the unitization results, while the x and y dimensions are chosen so that the resultant subvolume approximates a representative element volume (REV) of that unit (Figure 5).
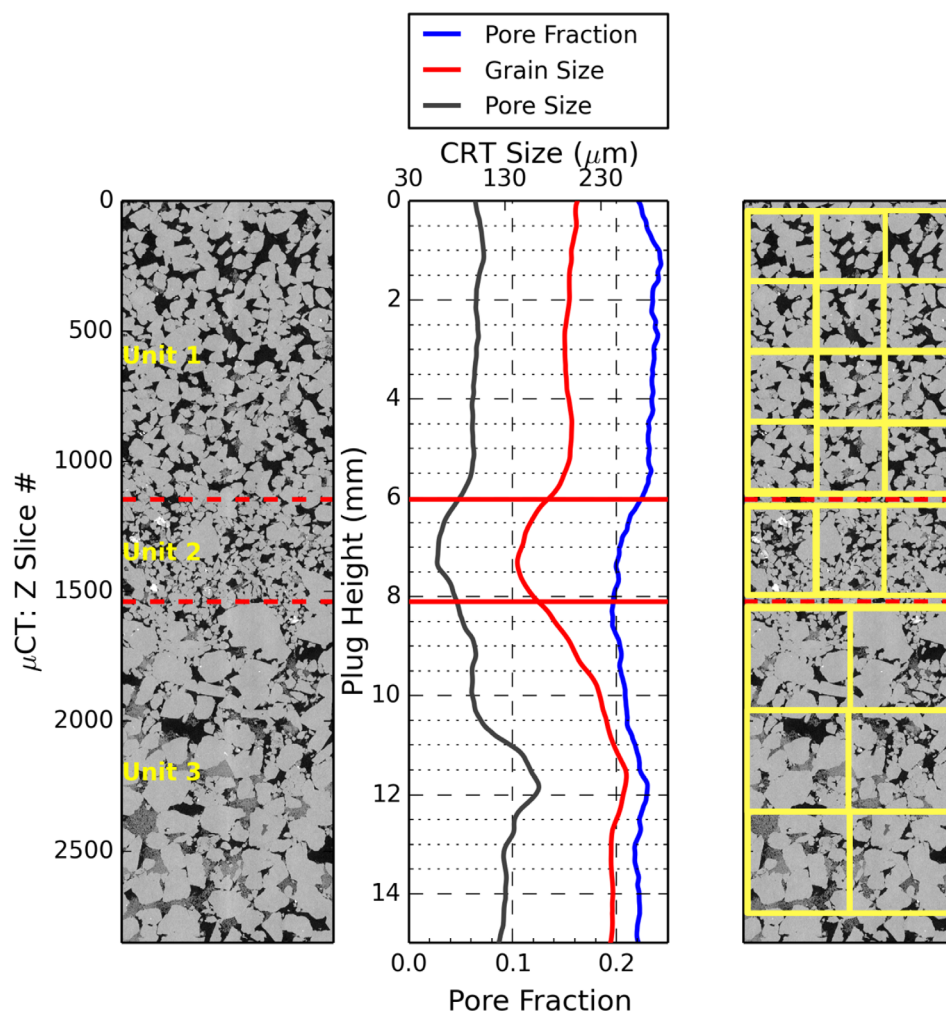
Figure 5. Unitization results for the 8 × 15 mm subplug (i.e., the field of view of the highest-resolution image). Horizontal red lines indicate boundaries identified from the grain size log. The yellow boxes indicate the subdivision of each unit into smaller subvolumes for individual permeability simulation and calculation of predictor characteristics. Identical subvolumes are used in computations at all three resolutions.

2.4. Computing Rock Characteristics

We compute a range of rock characteristics for each subvolume identified in the unitization step (section 2.3) and use these characteristics as predictor variables in statistical models of absolute permeability.

2.4.1. Grain and Pore Size and Sorting (GS, Gsort, PS, and Psort)

To compute grain and pore size and sorting, we use the segmented data to construct a Euclidean distance map, which, for each voxel, assigns a value equivalent to the shortest distance to a boundary voxel [*Danielsson*, 1980]. The distance map is further processed by a watershed transform [*Beucher and Meyer*, 1992], followed by merging of labeled watershed regions, which generates a partitioning of the grain or pore space into individual grains or pores [*Thompson et al.*, 2005; *Sheppard et al.*, 2006]. An analysis of regions volumes bins the resulting regions into size classes expressed in number of voxels, which we convert to equivalent sphere diameter (ESD) [*Jennings and Parslow*, 1988]. Assuming a log-normal distribution, a cumulative logarithmic ESD size distribution curve is used to calculate the median grain and pore size in microns for each subvolume [*Krumbein*, 1934]. We express grain and pore sorting as a measure of spread using the 5th, 16th, 84th, and 95th percentiles from the same size distribution curves [*Folk and Ward*, 1957].

2.4.2. Open Pore Fraction (OPF), Porosity (P), and Clay Fraction (CF)

Here we make use of the segmented data files that represent the original gray scale tomograms in terms of three classes representing (a) open pores as low brightness voxels, (b) clay and subresolution porosity as intermediate gray scale voxels, and (c) the grain phase as high brightness voxels (Figure 4b). Summing the number of voxels in each class and normalizing to the total number of voxels in the image gives the

fractional contribution of each class. Open pore fraction is the fraction of resolved void space clearly distinguished from the intermediate and grain phases. As mentioned in section 2.2 on image segmentation, we use a "soft" thresholding segmentation method, which allocates 100 gray scale values to the intermediate intensity voxels (Figure 4c). Based on a linear interpolation between a minimum and maximum gray scale value, we compute the fractions of clay phase and subresolution pores. By adding the fraction of subresolution pores to the open pore fraction, we determine the porosity value [*Sok et al.*, 2009].

2.4.3. Formation Factor (F)

We compute the formation factor by numerically solving Laplace's equation using a finite element or finite difference formulation to solve for the potential in a unity strength electrical field [*Arns et al.*, 2001a, 2002]. The electrical conductivity (S) of each gray scale voxel is given by *Archie*'s law $S = \phi^m$ where m is the cementation exponent and ϕ the porosity. Using conventional experimental data, the m exponent can be computed as the slope of a plot of the logarithm of formation factor and the logarithm of porosity. The numerical computation of formation factors requires a predetermined value for m. *Archie* [1942] found that m ranges between 1.8 and 2 for consolidated sandstone, and mentioned it can be as low as 1.3 for clean unconsolidated sands. We are specifically interested in testing if formation factor contributes significantly to a statistical model of permeability, because here the formation factor computation is tuned to take into account the scaled subresolution porosity data in the intermediate gray scale voxels. For this reason, especially in the case of low-resolution images, the result from the formation factor computation is not necessarily a reliable measure of electrical conductivity. Instead it is an arbitrary characteristic chosen for possible correlation with absolute permeability because it represents current flow through voxel space where resistance to flow at each voxel is determined by the fraction of pore space and intermediate clay phase in that voxel. To test the sensitivity of the correlation between formation factor and permeability to variations in the m exponent, we generate formation factor data for $m = 2, 2.5,$ and 4. We select 2 because it is the classically accepted value for consolidated sands, while higher values are considered because they may help to capture the fact that fluid flow is highly sensitive to obstructions.

2.4.4. Minkowski Functionals

The so-called Minkowski Functionals are a set of additive morphological measures representing, for three-dimensional objects, volume, surface area (SA), mean curvature (MC), and the Euler characteristic (EC) [*Mecke*, 1996; *Arns et al.*, 2001b; *Schladitz et al.*, 2006]. The volume measurement is equal to the open pore fraction explained in section 2.4.1. Here we generate data for the Minkowski Functionals using the morphological analysis algorithm implemented by *Arns et al.* [2001b], which includes the computation of the critical length (lc).

2.5. Statistical Modeling

The permeability prediction workflow involves two stages of statistical calibration based on the 8 mm subplug region in the three images. The first stage is the correlation between individual predictor character characteristics from the low and intermediate-resolution images with numerically computed permeability from the high-resolution image using ordinary least squares (OLS) linear regression. The second stage combines several characteristics in a multiple OLS linear regression to develop a more complete statistical description of the response variable (absolute permeability). In OLS, the coefficient of determination (R^2) is a measure of how much variance in the response variable can be explained by the predictor characteristics. R^2 is the difference between 1 and the ratio of the total sum of squares (SS_{res}) and the residual sum of squares (SS_{tot}) (equation (2)).

$$R^2 = 1 - \frac{SS_{res}}{SS_{tot}} \tag{2}$$

SS_{tot} is equal to the sum of the squares of the difference between the observed values and the mean of the observed values (response variable). SS_{res} is equal to the sum of the squares of the difference between the observed values and the predicted values of the model. R^2 ranges between 0 (no correlation between the predictors and the response variable) and 1 (the predictor characteristics perfectly describe the variability in the response variable). Based on 48 data points for each characteristic, we use R^2 as a measure of the predictive capability of individual rock characteristics, and to assess their relative contribution to predicting permeability in multiple linear models combining a subset of characteristics. Additionally, the F-statistic, expressed as a probability value (p-value), gives an indication if a model of the response variable is significantly different from a regression model with no predictor variables (intercept model).

As is typical in regression analysis when considering multiple predictors with a range of values in different units, we standardize each predictor by subtracting the mean and normalizing to its standard deviation [*Marquardt*, 1980].

In developing the statistical models used for permeability prediction, we first assess the predictive ability of each individual characteristic. The next step is to consider if some combination of variables in a multiple linear model provides a more complete description of the permeability variations. Critically we must consider which characteristics to include in such a multiple model. One method is to assess each single variable model and decide, based on R^2, the model p-value, and an understanding of the physical meaning of each characteristic, which combination of predictors are most likely to define a reliable model. Alternatively one could use a multivariate analysis technique such as principal component analysis (PCA). We perform a PCA on standardized variables since it aims to identify directions of maximum variance [*Jackson*, 2005]. The results include eigenvalues, the amount of variance, and eigenvectors, the principal components defining the direction of maximum variance. PCA of *n* variables produces *n* principal components, with each principal component a linear combination of the original variables [*Jolliffe*, 2014]. The "loadings" between each principal component and the original variables are computed using equation (3), and indicate how well each principal component is aligned with the original variables, i.e., how much information from each variable is reflected in each principle component [*Abdi and Williams*, 2010] (Please note that the popular statistics software package "R"' refers to eigenvectors as "loadings," which is distinct from the definition used here). The loadings between the principal components and the original variables may reveal which original characteristics are best suited to construct a predictive multiple OLS model. Furthermore, the principal components can be used as new predictor variables of the response variable in a principal component regression; however, in this instance, we choose not to make use of this regression method for statistical calibration, because the principal components cannot be interpreted directly in terms of their physical meaning.

$$r_{ij} = \frac{u_{ij}\sqrt{l_i}}{s_j} \tag{3}$$

where *r* is the correlation between the ith principal component and the jth original variable, *u* is the eigenvector coefficient, *l* is the eigenvalue, and *s* is the variance of the original variable, which is 1 for standardized data.

3. Results and Discussion: Sample 1

3.1. Permeability Estimation and Image Resolution

Whenever possible, one would determine permeability directly; indirect methods are required only when direct computation is impossible. In this section, we demonstrate that conventional methods of estimating permeability, such as Lattice-Boltzmann-based simulations and Katz-Thompson calculations, fail when there is not sufficient resolution in the image to accurately represent the pore space. Figure 6a shows how the loss of geometric information impacts computed permeability using the Lattice-Boltzmann method. The 16 μm/voxel image yields unreliable results, returning zero or underestimating the permeability compared to the 5 μm/voxel data for values lower than ∼2000 mD.

Figure 6b shows the good correlation between permeability computed using the Lattice- Boltzmann method and the Katz-Thompson equation for the 5 μm/voxel image. The resolution is sufficiently high to accurately represent the largest connecting pore throats and to allow reasonable estimates of the pore system critical length, and therefore its permeability using the Katz-Thompson method. Note that to achieve this correlation the universal constant in equation (1), reported as $\frac{1}{226}$ by *Katz and Thompson*, was modified to $\frac{1}{21}$. Computing the R^2 statistic for the 1:1 line (an indication of how closely the data points fall on the line passing through zero with a 45° angle) yields a value of 0.86, indicating the Lattice Boltzmann and Katz-Thompson computations match one-another closely. Figure 6c shows the permeability using the Lattice-Boltzmann method for the 5 μm/voxel image against the permeability computed using Katz-Thompson and the 16 μm/voxel image. In this instance, the universal constant was set to $\frac{1}{15}$. Note how the Katz-Thompson results for the 16 μm/voxel image returns zero permeability for several volumes. The lower image resolution is not sufficient to capture the permeability-controlling flow pathways, leading to zero
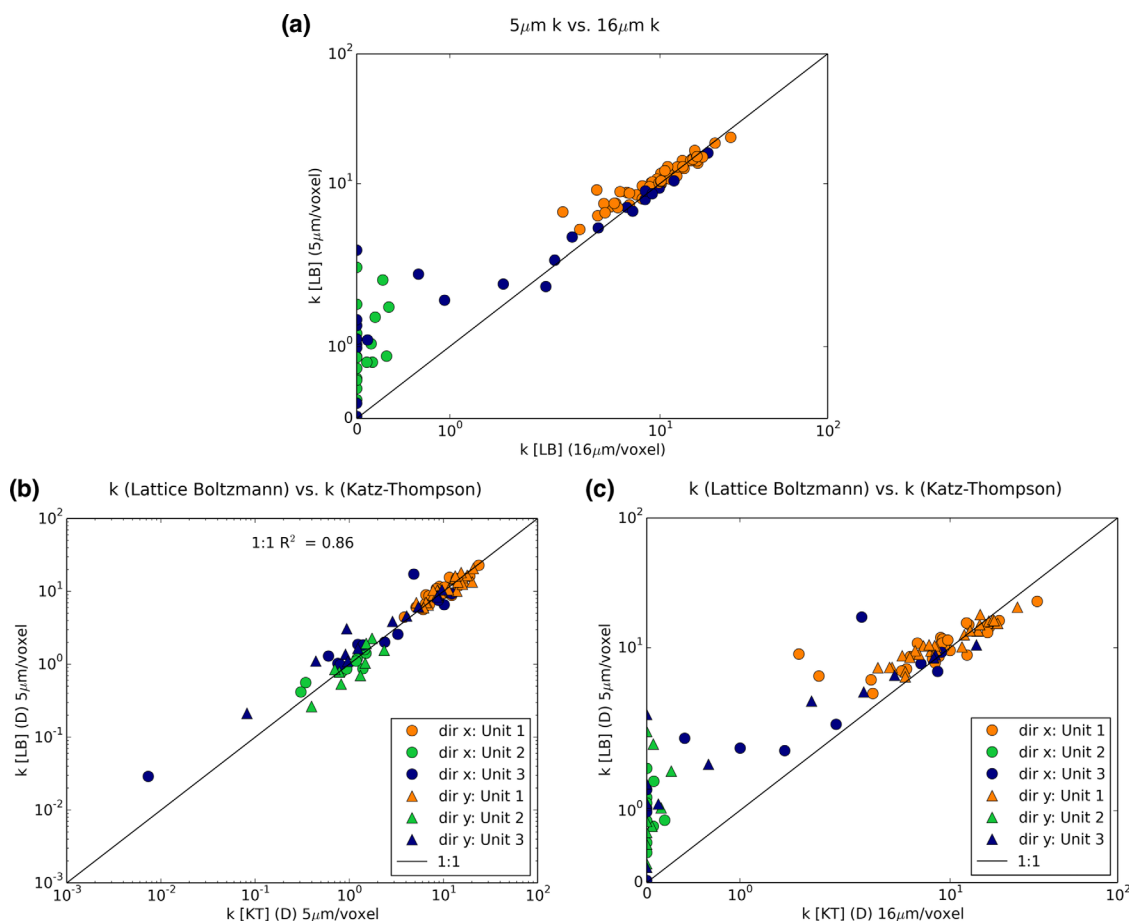
Figure 6. Using Katz-Thompson computed permeability to demonstrate why permeability simulations using the Lattice-Boltzmann method fail for lower resolution images. (a) Simulated permeability using the Lattice-Boltzmann method for the 5 and 16 μm/voxel images shows that the computation fails in the lower resolution image. (b) There is good agreement between computed permeability in the 5 μm/voxel image using the Lattice-Boltzmann and Katz-Thompson methods; however, (c) plotting permeability from the Lattice-Boltzmann method for the 5 μm/voxel image against Katz-Thompson permeability computed from the 16 μm/voxel image shows how several computation volumes in the 16 μm/voxel image have zero critical length, and therefore, zero computed permeability. Plotted with the "Matplotlib" python library with axis types set as "symlog," which provides logarithmic scales that include a small linear scale around zero, allowing zero to be plotted.

critical length values and zero computed permeability. It follows that for the 16 and 64 μm/voxel images of these samples both the Lattice-Boltzmann and Katz-Thompson methods cannot produce reliable results and we need an alternative method of determining permeability.

3.2. Statistical Calibration: Individual Characteristics

As a first step, we compile OLS models between the logarithm of each characteristic and the logarithm of permeability. The second stage of statistical calibration combines some subset of the individual characteristics into multiple linear models (section 3.3) to provide a more complete statistical description of permeability. One method of identifying predictor variables for a multiple OLS linear model is a principal component analysis. The results from the PCA (Table 1) show that the first three principal components explain 90% of the variance in the predictor characteristics for both the 16 and 64 μm/voxel images. For the 16 μm/voxel data, the first two principal components, PC1 and PC2, correlate well with permeability based on their R^2 values. The loadings for the 16 μm/voxel data indicate that PC1 shares considerable information with open pore fraction, porosity, formation factor, grain sorting, clay fraction, and mean curvature, while PC2 shares information with pore and grain size and pore sorting. For the 64 μm/voxel image, PC1 correlates best with permeability. The loadings of PC1 show a similar trend compared to that of 16 μm/voxel image, but with the addition of the Euler characteristic, which also shares considerable information with the first principal component.

Table 1. Principal Component Analysis Results for the 16 and 64 μm/voxel Data Showing the Coefficient of Determination (R^2) Between the First Three Principal Components and Permeability, the Fraction of Variance Explained by the Components, and the Loadings (Correlations) of the Components Onto the Original Variables

	R^2 w. Perm.	Variance Fraction	OPF	P	PS	F	GS	Gsort	Psort	CF	SA	MC	EC
16 μm/voxel image													
PC1	0.8	0.6	−0.9	−0.9	−0.5	0.8	0.0	0.9	0.1	0.9	−1.0	−0.9	1.0
PC2	0.7	0.2	0.3	0.1	−0.8	0.2	−0.9	0.0	−0.8	−0.4	0.0	−0.3	0.0
PC3	0.3	0.1	0.3	0.3	−0.1	−0.3	−0.3	0.3	0.6	0.1	−0.1	−0.2	0.1
64 μm/voxel image													
PC1	0.8	0.5	−0.9	−0.3	−0.6	0.9	0.2	0.7	−0.4	−0.3	−1.0	−0.9	0.9
PC2	0.2	0.3	0.2	0.9	−0.6	−0.2	−0.9	0.1	−0.3	0.9	−0.1	−0.4	0.1
PC3	0.1	0.1	0.1	−0.2	−0.2	0.1	0.0	−0.2	−0.8	−0.1	0.2	0.1	−0.2

Another method of choosing the characteristics for a multiple regression model is to consider the predictive capability of the individual characteristics by interpreting the coefficient of determination from OLS regressions (Table 2). Based on the R^2 statistic, the characteristics relating to rock fabric in neither the 16 nor 64 μm/voxel images correlate well with permeability, while specifically open pore fraction and formation factor, which relate more directly to the pore system, show much stronger correlations. Mean curvature, surface area, and the Euler Characteristic correlate reasonably well and justify further investigation. Each model's p-value of the F-statistic is lower than 0.05. With a chosen significance threshold of 95%, the p-values indicate that each model has less than 5% probability of being equal to the intercept model; therefore, each individual characteristic provides a statistically significant description of permeability variance.

We now choose the most suitable predictor characteristics based on the combined results of the principal component analysis and the regression for each individual characteristic with permeability.

3.2.1. Rock Fabric

In unconsolidated sands, grain size, grain sorting, and packing structure have fundamental control over the pore system, and have shown strong correlation with permeability [*Krumbein and Monk*, 1943; *Berg*, 1970; *Chapman*, 1981; *Detmer*, 1995]. However, diagenetic and lithification processes, such as chemical dissolution, recrystallization of minerals, and compaction alter the flow properties in consolidated systems [*Hayes*, 1979]. Even though the PCA results show that grain size and sorting align well with the main principal components, Table 2 indicates that Precipice Sandstone grain properties do not correlate well with permeability. One could argue that such rock properties have a significant influence on fluid flow; however, the relationships between these simple measurements of fabric properties and permeability are not evident in this data set. In the remainder of the paper, we focus on those characteristics that relate more directly to the pore system and show stronger individual correlation with computed permeability.

3.2.2. Open Pore Fraction, Pore Size, and Formation Factor

The PCA results show that open pore fraction and formation factor share considerable information with the first principal component in both image resolutions (Table 1). Table 2 indicates that these are the characteristics that correlate best with permeability, for both 16 and 64 μm/voxel images. R^2 for the correlation between open pore fraction and permeability is lower in the 5 μm/voxel image, compared to the 16 and 64 μm/voxel images.
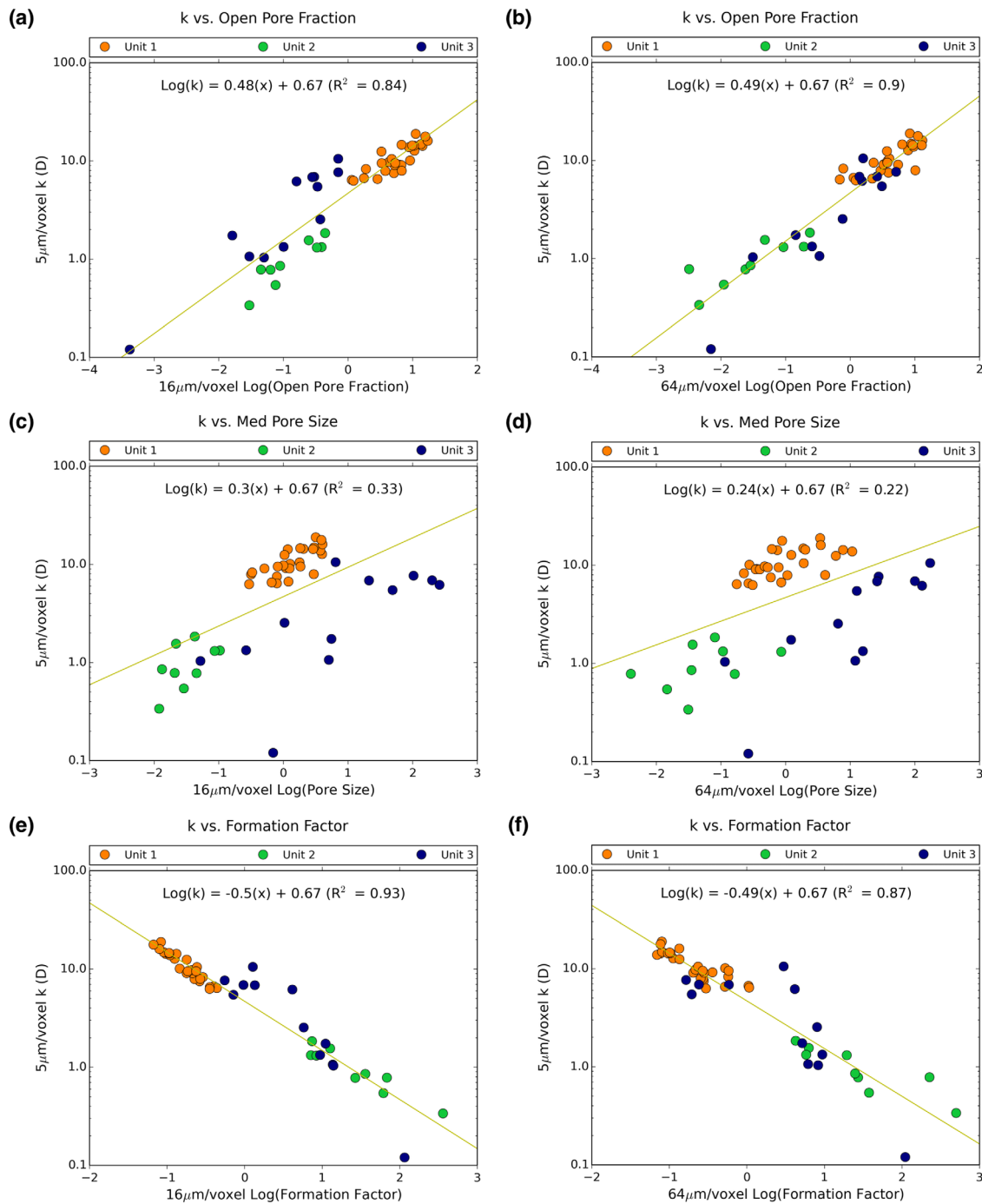
Table 2. The Coefficient of Determination From Ordinary Least Squares Modeling of Each Calculated Characteristic (From the 5, 16, and 64 μm/voxel Images) With Lattice Boltzmann Permeability From the 5 μm/voxel Image

Characteristic	R^2 for log (k) Versus log (5 μm/voxel Characteristics)	R^2 for log (k) Versus log (16 μm/voxel Characteristics)	R^2 for log (k) Versus log (64 μm/voxel Characteristics)
Rock fabric			
Grain size (GS)	0.114	0.018	0.206
Grain sorting (Gsort)	0.556	0.544	0.275
Clay fraction (CF)	0.393	0.542	0.286
Pore system			
Porosity fraction (P)	0.612	0.780	0.221
Open pore size (μm) (PS)	0.564	0.332	0.216
Open pore sorting (Psort)	0.103	0.019	0.033
Formation factor (m = 2) (F)	0.770	0.932	0.871
Formation factor (m = 2.5) (F)	0.754	0.931	0.850
Formation Factor (m = 4) (F)	0.740	0.928	0.875
Minkowski functionals			
Open pore fraction (OPF)	0.567	0.841	0.899
Surface area (SA)	0.071	0.770	0.643
Mean curvature (MC)	0.555	0.719	0.488
Euler characteristic (EC)	0.187	0.752	0.626

Figure 7. (a and b) The correlations between permeability and open pore fraction, (c and d) open pore size, and (e and f) formation factor calculated from the 16 and 64 μm/voxel images.

Figures 7a and 7b plot simulated permeability against open pore fraction for the 16 and 64 μm/voxel images of the 8 mm subplug. The correlation is relatively poor at 5 μm/voxel image resolution since relevant factors such as the length scale and connectedness of the pore system make no direct contribution to the open pore fraction characteristic. However, at lower image resolutions, open pore fraction is no longer a direct measure of sample porosity, but rather the resolved fraction of the larger actual pore volume; i.e., pores larger than some resolution-dependent length cutoff. Figure 7b demonstrates an excellent correlation between open pore fraction and permeability in the 64 μm/voxel images. We postulate that when the resolution is such that the length
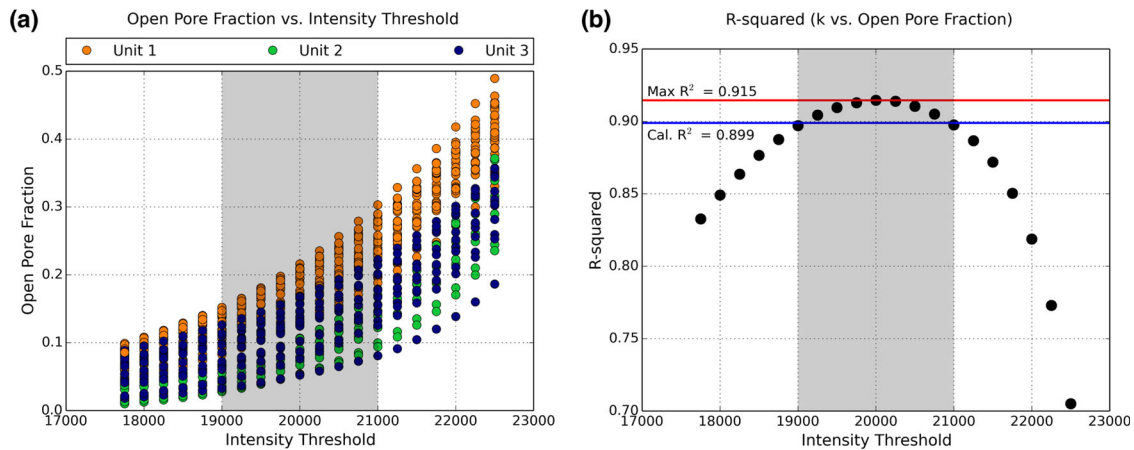
Figure 8. (a) Open pore fraction as a function of the gray scale threshold value; (b) the correlation R^2 between permeability and open pore fraction as a function of the gray scale threshold. The shaded areas show the range of gray scale values over which permeability remains highly correlated to open pore fraction, indicating that the statistical model is relatively independent of the image segmentation parameters.

cutoff is close to a controlling length scale of the pore system (e.g., the critical length), then the fraction of open pore space correlates well to the number of transport pathways relevant for permeability.

The correlation coefficient for pore size shows that it is a stronger predictor characteristic in the 16 μm/voxel image, which retains more geometric information compared to the 64 μm/voxel image (Table 2 and Figures 7c and 7d). Even though the pore-size correlation coefficient is relatively low, being the only direct measure of size in these low-resolution images it may contribute to the statistical description of permeability in a multiple model, and we choose to include it in the subset of characteristics for further analysis.

Formation factor represents relative electrical conductivity; however, in low-resolution images, where electrical flow paths are poorly characterized, formation factor computations do not provide reliable information on the electrical properties of the rock. In this study, we see similar results than those of *Arns et al.* [2001a] with higher computed formation factor for lower-resolution images. Additionally, the correlation coefficient between formation factor computed on the 5 μm/voxel image and that from the 16 and 64 μm/voxel images is 0.5 and 0.3, respectively, indicating that formation factor is poorly correlated with itself between image resolutions. Here the formation factor computation is tuned to take into account the scaled microporosity information contained in the gray scale value of each intermediate voxel. Computation results with $m = 2$, 2.5, and 4 show only minor differences in the correlation coefficients when modeled against permeability (see section 2.4.3 for a discussion on why we selected these values for m). For each value of m, the correlation coefficient for formation factor is lowest in the 5 μm/voxel image and highest in the 16 μm/voxel image. We suggest that in the lower resolution images, the formation factor computation appears to incorporate some measure of connecting channel size from image gray scales and therefore becomes a reasonable predictor of permeability (Figures 7e and 7f). Additionally, when computing gray scale sensitive formation factor values in lower resolution images, the smaller pores, which contribute to permeability but which are not fully resolved in lower resolution images, are still taken into account because they are represented as intermediate gray scale values. It is expected that the range of resolutions for which formation factor is a useful predictor will vary between samples as a function of rock texture.

3.2.3. Sensitivity to Segmentation Parameters

Open pore fraction is directly dependent on the image gray scale segmentation threshold, so the sensitivity of this promising correlation to the threshold parameter should be explored. Figures 8a and 8b show open pore fraction from the 64 μm/voxel image and its correlation with permeability as a function of simple gray scale thresholding. As the threshold increases, the open pore fraction and its range increase indefinitely as more voxels are included in the segmented pore phase. The correlation coefficient with permeability increases to a maximum and then decreases. The maximum R^2 of 0.915 is very similar to the R^2 of 0.899 (reported in Table 2), indicating that the component of the pore system that correlates well with permeability can be captured over a

Table 3. The Coefficient of Determination From Ordinary Least Squares Modeling of Five Combinations of Predictor Characteristics (From the 5, 16, and 64 μm/voxel Images) with Lattice Boltzmann Permeability From the 5 μm/voxel Image

Multiple Model	R^2 for log (k) Versus log (5 μm/voxel Characteristics)	R^2 for log (k) Versus log (16 μm/voxel Characteristics)	R^2 for log (k) Versus log (64 μm/voxel Characteristics)
1) OPF, F	0.843	0.932	0.908
2) OPF, PS, F	0.965	0.963	0.912
3) SA, MC, EN	0.696	0.777	0.677
4) OPF, SA, MC, EN	0.830	0.955	0.922
5) SA, MC, EN, F	0.910	0.953	0.875
6) OPF, PS, F, SA, MC, EN	0.971	0.969	0.927

relatively large range of gray scale thresholds. This result indicates that the predictive model based on open pore fraction is relatively independent of the segmentation parameters used for the low-resolution image.

3.3. Statistical Calibration: Multiple Characteristics

Combining predictor characteristics into multiple linear models has the potential to improve predictive capabilities and serves as the second step in calibrating the statistical models. Based on the results from the principal component analysis and the regression of each characteristic with permeability, we suggest that some combination of open pore fraction, pore size, formation factor, and the Minkowski Functionals are likely to generate good multiple linear models of absolute permeability. We emphasise that the intention is to develop a workflow rather than an empirical model for predicting permeability. It is possible that other samples will require different statistical models depending on their textures and the image resolution.

Table 3 shows six multiple models and their R^2 values for regressions using characteristics from the 5, 16, and 64 μm/voxel images. Each model's p-value of the F-statistic is lower than 0.05, indicating that each model is significantly different from the intercept model. The two best individual characteristics are open pore fraction and formation factor, and a multiple linear model containing both (model 1) provides an excellent description of permeability, especially in the 16 μm/voxel image. Even though pore size alone does not appear to contain any significant predictive capability (Table 2 above), adding it to model 1, to produce multiple model 2, significantly increases the correlation coefficient in the 16 mμm/voxel image. This is not true for the 64 μm/voxel data, where adding pore size to model 1 only increases the R^2 by 0.004. This indicates that at low-resolution the pore size characteristic no longer has any predictive capability, showing that the 64 μm/voxel image contains no direct geometric information that contributes to a model for permeability. Instead the pore geometry is now represented by intermediate gray scale values and is accounted for by the formation factor, which incorporates gray scales during computation.

As individual characteristics the Minkowski functionals generate promising R^2 values, particularly for the 16 μm/voxel image (Table 2 above). However, when combined in model 3, the correlation coefficient is less impressive at 0.8, 0.78, and 0.67 for the 5, 16, and 64 μm/voxel images, respectively. Only when open fraction or formation factor is added to surface area, mean curvature, and the Euler Characteristic in models 4 and 5 does the R^2 improve. Furthermore, model 6 contains open pore fraction, pore size, and all three of the remaining Minkowski Functionals, and produces an R^2 of 0.968 and 0.927 for the 16 and 64 μm/voxel data, which is only marginally better than the correlation coefficients for models 1 and 2. It is therefore clear that the Minkowski Functionals do not contribute additional information to a multiple model, which is not already accounted for by open pore fraction, pore size, and formation factor. Based on the results in Table 3, we therefore identify models 1 and 2 for use in predicting permeability in the 25 mm 64 and 16 μm/voxel images, respectively.

The coefficient of determination alone, though a valuable measure of precision, cannot be used to determine the quality of a model. Model residuals (the differences between the predicted and observed values) should ideally show a random distribution around zero with no clustering of the data points and no clearly discernable patterns, the presence of which may point to some systematic bias in the model [*Draper and Smith*, 2014]. Figure 9a shows the simulated permeability from the 5 μm/voxel image plotted against the predicted permeability from the 16 μm/voxel image using multiple linear model 2 (open pore fraction, open pore size, and formation factor). Figure 9b shows the model residuals plotted against the predicted values. Figured 9c and 9d show similar data for the 64 μm/voxel image obtained from model 1 (open pore fraction and formation factor). Upon visual inspection, we note the residuals in Figures 9b and 9d show relatively random distributions indicating that a linear model is unbiased and appropriate for the data. There are a few data points at lower permeabilities with higher residual values, which we suggest is a
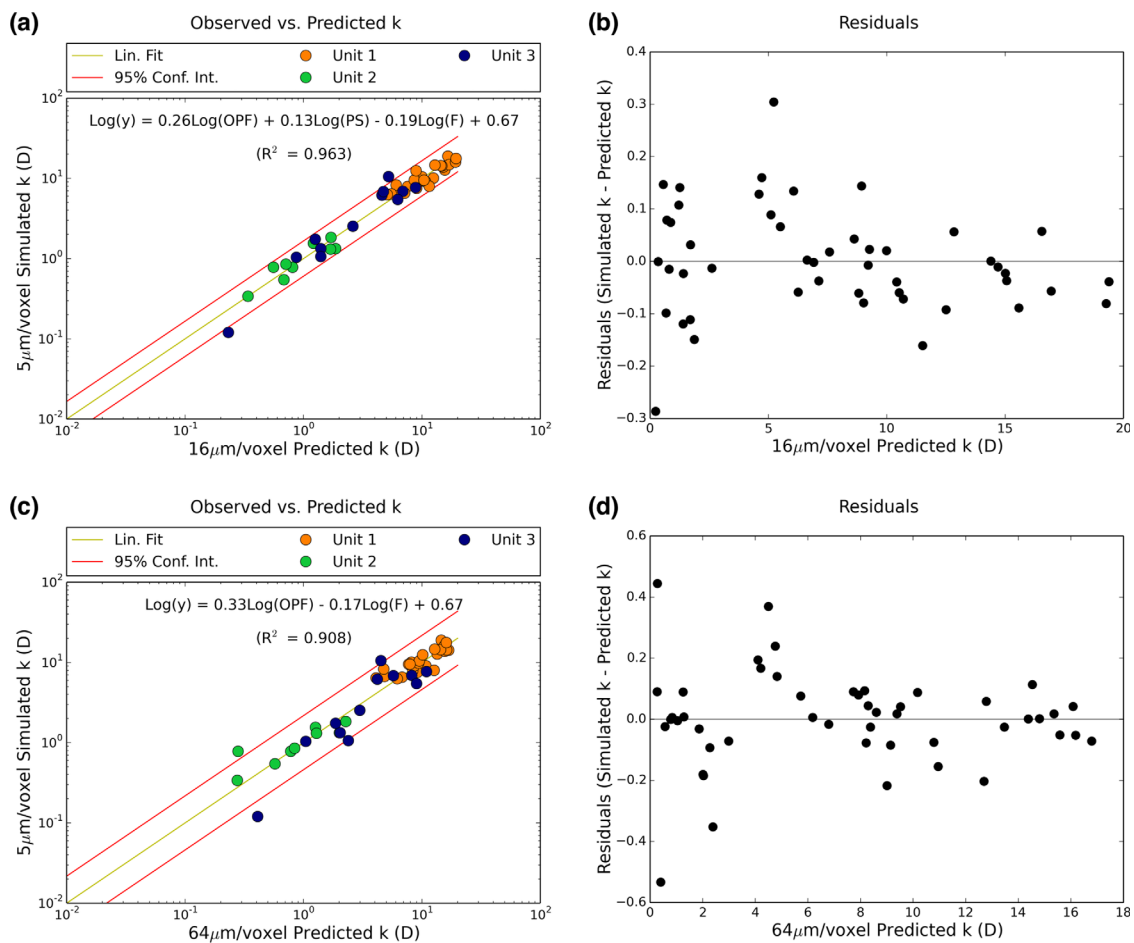
Figure 9. Calibration of statistical models over the small field of view of the highest resolution image. (a) The simulated permeability from the 5 μm/voxel image plotted against the predicted permeability from the multiple model containing open pore fraction, open pore size, and formation factor from the 16 μm/voxel image and (c) open pore fraction and formation factor from the 64 μm/voxel image. (b and d) Multiple linear model residuals plotted against the predicted permeability values have no apparent systematic bias.

consequence of the low-permeability data being more scattered. It also shows the difficulty of predicting lower permeability values (<1000 mD) from such low-resolution images.

3.4. Predicting Permeability in the 25 mm Core Plug

The last step in the workflow is to predict permeability from the images of the full 25 × 80 mm core plug. Using the statistical calibration of model 1 (open pore fraction and formation factor) for the 64 μm/voxel image and model 2 (open pore fraction, open pore size, and formation factor) for 16 μm/voxel image, Figure 10 shows the predicted absolute permeability for the 25 mm core plug from both image resolutions. As before, the predictor characteristics are computed on several subvolumes within each unit separately. Figure 10 shows a single value permeability for each rock unit, which is the average of the predicted permeability of the subvolumes. Certain sections in the core plug such as units 2 and 3 show relatively high permeability, despite their fine-grained rock fabric and apparently closed pore systems compared to that of units 11 and 12.

The best imaging resolution that could be achieved over the full 25 × 80 mm volume was 16 μm/voxel, a data set of 1800 × 1800 × 5000 voxels, which was insufficient to allow direct simulation of permeability. In the absence of accurate direct simulations, and having achieved excellent statistical permeability predictions from the 16 μm/voxel calibration data (Figure 9a), we use the predicted permeability over the full 25 × 80 mm volume as a proxy for directly computed permeability. Comparisons between predicted permeability for the 8 mm subplug (the calibration volume) and 25 mm core plug are shown in Figure 10. The 1:1 R^2 values show that predictions from the low-resolution 64 μm/voxel image match those from the 16 μm/
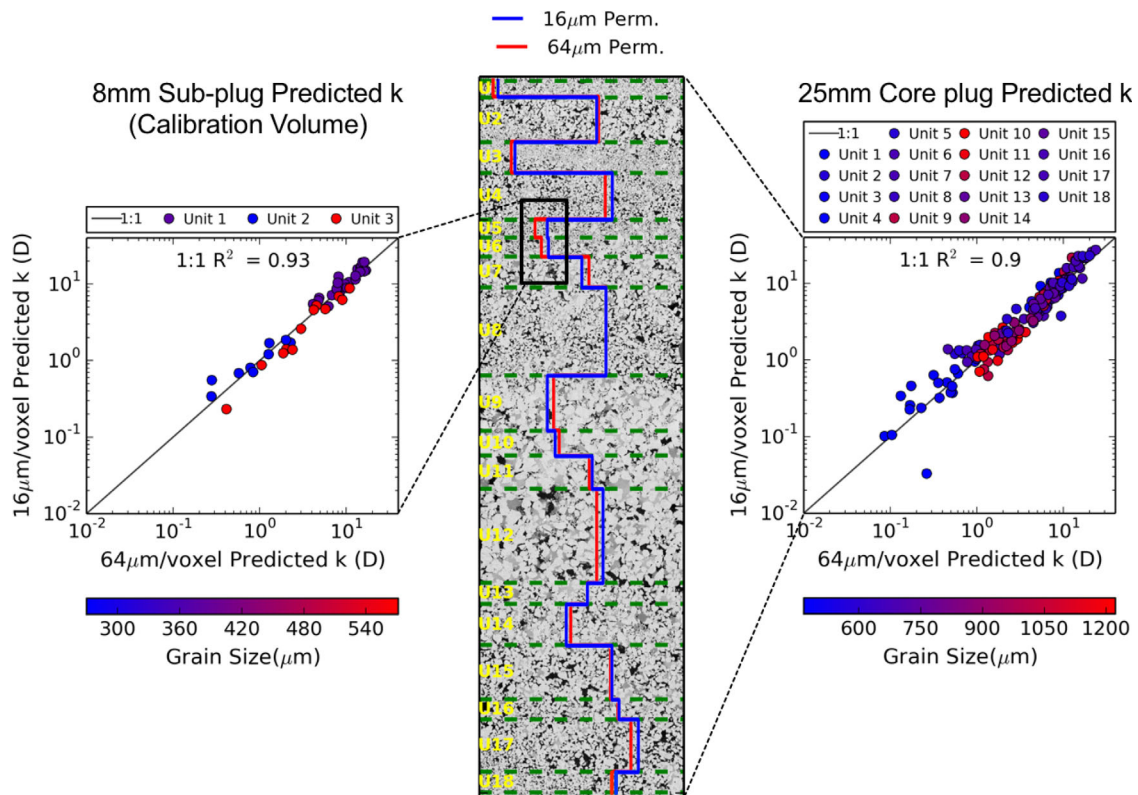
Figure 10. The predicted permeability of the 25 mm core plug computed from multiple linear model 2 (open pore fraction, open pore size, and formation factor) for the 16 μm/voxel image, and multiple linear model 1 (open pore fraction and formation factor) for the 64 μm/voxel image. Green horizontal stippled lines indicate the boundaries between rock units and the black box indicates the approximate location of the 8 mm subplug. The scatterplots compare the predicted permeabilities from the 16 and 64 μm/voxel images for (left) the 8 mm subplug calibration volume and (right) the 25 mm core plug.

voxel image very well for both the 8 × 15 mm calibration volume ($R^2 = 0.93$) and the as-yet-unexplored 25 × 80 mm volume ($R^2 = 0.90$). This is an exciting result since two different statistical models, applied to two images with different resolutions, predict very similar permeabilities.

As a word of caution, we emphasize that the high-resolution data from the 8 mm subplug underpins the permeability predictions made over the full 25 × 80 mm volume from the 16 and 64 μm/voxel images. If the subplug does not represent an adequate range of rock textures, so that significant extrapolation of the statistical model is required beyond the range of rock characteristics captured in the 8 mm subplug, then uncertainties in the predicted permeability are bound to increase. Future research will need to look into this aspect in more detail. An approach likely to provide some quantitative data is to collect a second subplug from a different location, and test the predicted permeability over the whole 25 mm core plug from the two calibration volumes.

4. Results and Discussion: Sample 2

After initial development of the workflow, we apply it to sample 2, another Precipice core sample of similar character to sample 1. We follow the same imaging protocols and perform the statistical calibration on a separate 8 mm subplug image collected from the new sample. Figure 11 shows statistical calibration data for the intermediate resolution 16 μm/voxel image (Figure 11a) and the low-resolution 61 μm/voxel image (Figure 11b). Notably the R^2 of the models are not as high as for the first sample; however, they appear good enough to suggest that the low-resolution images contain the relevant information on the pore system to allow permeability prediction.

We suggest that the main cause of the poor correlations is related to the quality of the high-resolution image used for permeability computation. Here the high-resolution image was not collected on a physically cored subplug, but rather as a "region of interest scan," which means that the high-resolution image was
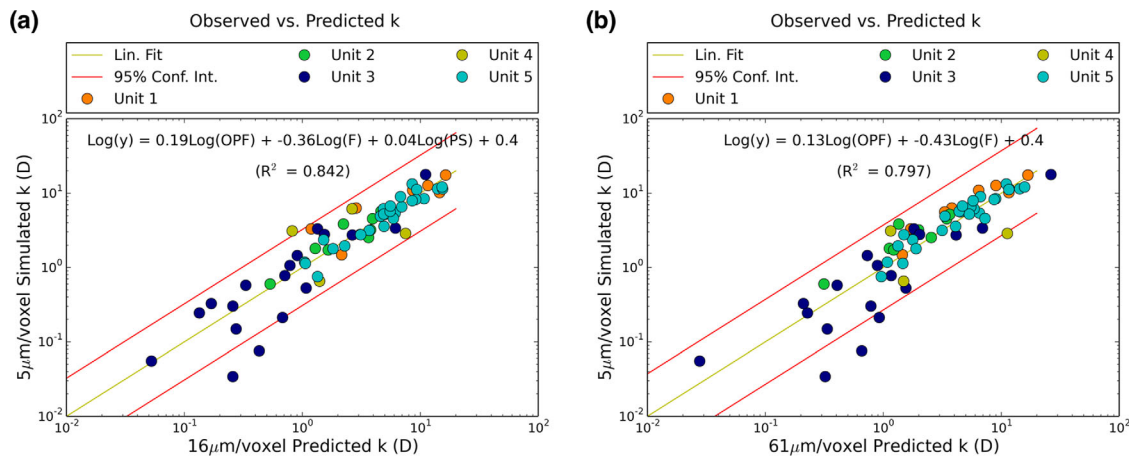
Figure 11. Calibration of statistical models for sample 2. The simulated permeability from the 5 μm/voxel image plotted against the predicted permeability from (a) the 16 μm/voxel image and (b) the 61 μm/voxel image.

collected by physically positioning the original large-scale sample closer to the X-ray source, thereby reducing the field of view and increasing the image resolution. This technique reduces the contrast-to-noise ratio in the high-resolution image (Figure 12a), directly impacting image segmentation. Most notably the pore space contains isolated groups of nonpore voxels (Figure 12b), which in turn impact the permeability computation because nonpore voxels do not allow fluid flow. The result is less reliable permeability data for calibration leading to poorer statistical correlations.

To test this hypothesis, we compute a new set of permeability data using a microporosity segmented image; specifically we set the first 26 gray scale values of the 100 intermediate gray scale voxels to permit fluid flow as if they were open pore voxels, thereby removing the negative effect of some of the isolated nonpore voxels (Figure 12c). The calibration results using this new set of permeability data show significant improvement and give R^2 values of 0.93 and 0.91 for the 16 and 61 μm/voxel images, respectively (Figured 13a and 13b). The 1:1 comparisons of the predicted permeability data are nearly as good as for sample 1 (Figure 13c and 13d), showing that 16 and 61 μm/voxel models produce similar predicted permeability values. This result demonstrates that image quality and the resultant computed permeability directly impact the statistical calibrations and the quality of the predicted data.

Samples 1 and 2 presented in this paper contain a wide range of rock textures from fine to coarse-grained, which makes them ideal for testing correlations between rock characteristics and petrophysical properties. However, both samples are from the same formation of sandstone, which may limit the generality of the results. Further work is required to fully understand the impact of the choice of subplug location and whether or not similar relationships exist in samples from other sandstone formations.
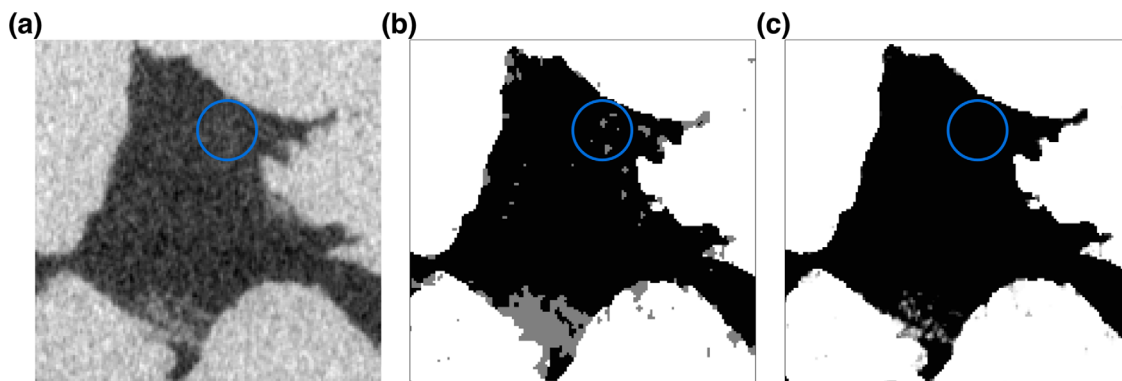

Figure 12. (a) A 2-D slice from the original tomogram showing the presence of noise, (b) the segmented image of the same area showing isolated clusters of nonpore voxels in the pore space, (c) a slice of the microporosity segmented image where the first 26 gray scale values are set to permit fluid flow.
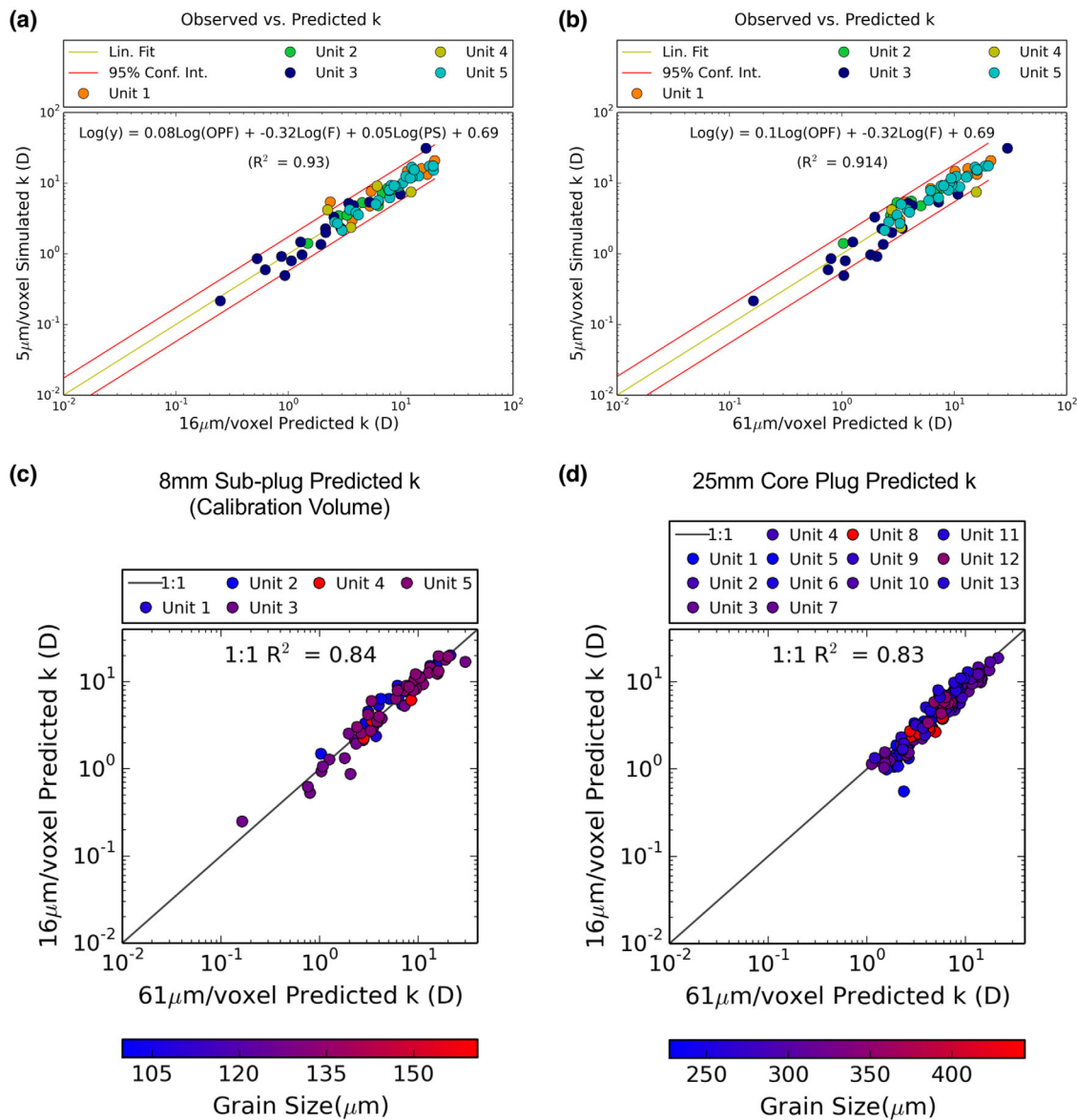
Figure 13. (a) The simulated permeability from the 5 μm/voxel image plotted against the predicted permeability from the 16 μm/voxel image and (b) the 61 μm/voxel image making use of a microporosity segmentation to adjust the permeability computation. Comparing the predicted permeability for (c) the 8 mm subplug and (d) the 25 mm core plug.

5. Conclusions

Large-scale whole core images often capture a range of rock textures and heterogeneities; however, they do not always have sufficient resolution to allow direct numerical simulations of fluid flow properties, and laboratory analysis of large quantities of core samples are not always practical or cost effective. We show that it is possible to use rock characteristics, namely open pore fraction, open pore size, and formation factor in a multiscale statistical modeling workflow to make good indirect predictions of permeability variation in low-resolution whole core images where it cannot be computed directly. The workflow produces a 3-D permeability map for large-scale core images, which is ideally suited for permeability upscaling and the computation of effective permeability at the core scale.

It can be inferred from our results that the open pore fraction and formation factor characteristics appear to capture critical aspects of the pore system when computed on images with relatively low resolution. The resolution is, in fact, far lower than that required to capture the full pore system in black-and-white. Open pore fraction is no longer a measure of porosity in these lower-resolution images and appears to relate to the

number of transport pathways critical to fluid flow. Critically, the correlation coefficient of the statistical model between permeability and open pore fraction remains relatively unchanged over a reasonable range of gray scale thresholds used for image segmentation. Formation factor, because of the use of gray scale information in its computation, seems to incorporate some measure of pore system length scale and connectedness.

We emphasise that further research is required to assess the general applicability of the results presented in this paper. Additional work should test the degree to which the choice of subplug location impacts on the predicted permeability results and to what extent a single calibration can be transferred to other samples collected from the same or different formations. Additionally, the quality of the statistical calibrations should be assessed on a sample-by-sample basis before any predictions are made at the larger scale. It is likely that there is a relatively narrow range of image resolution for which the characteristics identified in this paper are effective predictors of permeability for a given rock. If the resolution is too high, then open pore fraction and formation factor do not contain information on channel sizes; if the resolution is too low, then pore system geometric information is lost altogether. Nevertheless, the approach presented here allows for permeability estimation for images of significantly lower resolution than was hitherto possible, and opens up the possibility of estimating permeability for whole-core digital images, since scanners exist today which can image whole core of 100 mm diameter at the ∼64 µm/voxel resolution used in this study.

In more complex rocks with more varied clay mineral composition and where the pore system connects in a different way, it is possible that the characteristics used in this study lose some of their value as predictors of permeability. For example, intermediate gray scale values representing pore throats and those representing clay minerals could easily be confounded, potentially compromising the statistical models. In the workflow presented here, these cases would be identified by poor cross-scale correlations during the statistics calibration stage. We also show that image quality and the associated quality of the reference computed permeability values are of critical importance to the reliability of the predicted permeability.

References

Abdi, H., and L. J. Williams (2010), Principal component analysis, *Wiley Interdiscip. Rev. Comput. Stat.*, *2*(4), 433–459, doi:10.1002/wics.101.

Apourvari, S. N., and C. H. Arns (2014), An assessment of the influence of micro-porosity for effective permeability using local flux analysis on tomographic images, in *Society of Petroleum Engineers - International Petroleum Technology Conference 2014, IPTC 2014, Unlocking Energy Through Innovation, Technology and Capability,* pp. 2049–2058.

Archie, G. E. (1942), The electrical resistivity log as an aid in determining some reservoir characteristics, *Trans. AIME*, *146*(01), 54–62, doi:10.2118/942054-G.

Arns, C. H., M. A. Knackstedt, M. V. Pinczewski, and W. B. Lindquist (2001a), Accurate estimation of transport properties from microtomographic images, *Geophys. Res. Lett.*, *28*(17), 3361–3364, doi:10.1029/2001GL012987.

Arns, C. H., M. A. Knackstedt, W. Pinczewski, and K. R. Mecke (2001b), Euler-Poincaré characteristics of classes of disordered media, *Phys. Rev. E*, *63*(3), 031112, doi:10.1103/PhysRevE.63.031112.

Arns, C. H., M. Knackstedt, W. Pinczewski, and E. Garboczi (2002), Computation of linear elastic properties from microtomographic images: Methodology and agreement between theory and experiment, *Geophysics*, *67*(5), 1396–1405, doi:10.1190/1.1512785.

Arns, C. H., M. A. Knackstedt, W. V. Pinczewski, and N. S. Martys (2004), Virtual permeametry on microtomographic images, *J. Pet. Sci. Eng.*, *45*(1–2), 41–46, doi:10.1016/j.petrol.2004.05.001.

Arns, C. H., M. A. Knackstedt, and N. S. Martys (2005), Cross-property correlations and permeability estimation in sandstone, *Phys. Rev. E*, *72*(4), 046304, doi:10.1103/PhysRevE.72.046304.

Aubertin, M., and R. P. Chapuis (2003), Predicting the Coefficient of Permeability of Soils Using the Kozeny-Carman Equation, École polytechnique de Montréal, Montréal.

Bell, B. A. (2001), A Review of basic core analysis techniques for proper evaluations of heavy oil reservoirs, in *Geology of the Midway-Sunset Oil Field and Adjacent Temblor Range, San Joaquin Basin, California*, pp. 243–246, Am. Assoc. of Pet. Geol., Pacific Section, Bakersfield, Calif.

Benavente, D., C. Pla, N. Cueto, S. Galvañ, J. Martínez-Martínez, M. A. García-del-Cura, and S. Ordóñez (2015), Predicting water permeability in sedimentary rocks from capillary imbibition and pore structure, *Eng. Geol.*, *195*, 301–311, doi:10.1016/j.enggeo.2015.06.003.

Berg, C. F. (2012), Re-examining *Archie*'s law: Conductance description by tortuosity and constriction, *Phys. Rev. E Stat. Nonlin. Soft Matter Phys.*, *86*(4 Pt 2), 046314.

Berg, C. F. (2014), Permeability description by characteristic length, tortuosity, constriction and porosity, *Transp. Porous Media*, *103*(3), 381–400, doi:10.1007/s11242-014-0307-6.

Berg, R. R. (1970), Method for determining permeability from reservoir rock properties, *Trans. Gulf Coast Assoc. Geol. Soc.*, *20*, 303–335.

Beucher, S., and F. Meyer (1992), The morphological approach to segmentation: The watershed transformation, in *Mathematical Morphology in Image Processing,* vol. 34, pp. 433–481, Marcell Dekker Inc., N. Y.

Blunt, M. J., B. Bijeljic, H. Dong, O. Gharbi, S. Iglauer, P. Mostaghimi, A. Paluszny, and C. Pentland (2013), Pore-scale imaging and modelling, *Adv. Water Resour.*, *51*, 197–216, doi:10.1016/j.advwatres.2012.03.003.

Botha, P. W. S. K., A. Golab, Bhattad, C. Goodwin, and A. P. Sheppard (2014), Multi-scale imaging and cross-property correlations in heterogenous sandstone, in *International Symposium of the Society of Core Analysts*, Avignon, France.

Brinkman, H. C. (1949), A calculation of the viscous force exerted by a flowing fluid on a dense swarm of particles, *Appl. Sci. Res.*, *1*(1), 27–34, doi:10.1007/BF02120313.

Carman, P. C. (1956), *Flow of Gases Through Porous Media*, Academic, N. Y.

Chapman, R. E. (Ed.) (1981), *Geology and Water*, Springer, Dordrecht, Netherlands.

Clennell, M. B. (1997), Tortuosity: A guide through the maze, *Geol. Soc. Spec. Publ.*, *122*(1), 299–344, doi:10.1144/GSL.SP.1997.122.01.18.

Cnudde, V., and M. N. Boone (2013), High-resolution X-ray computed tomography in geosciences: A review of the current technology and applications, *Earth Sci. Rev.*, *123*, 1–17, doi:10.1016/j.earscirev.2013.04.003.

Danielsson, P.-E. (1980), Euclidean distance mapping, *Comput. Graph. Image Process.*, *14*(3), 227–248, doi:10.1016/0146-664X(80)90054-4.

Dehghan Khalili, A., J.-Y. Arns, F. Hussain, Y. Cinar, W. Pinczewski, and C. H. Arns (2013), Permeability upscaling for carbonates from the pore scale by use of multiscale X-ray-CT images, *SPE Reserv. Eval. Eng.*, *16*(4), 353–368, doi:10.2118/152640-PA.

Detmer, D. M. (1995), Permeability, porosity, and grain-size distibrution of selected Pliocene and Quaternary sediments in the Abuquerque Basin, *N. M. Geol.*, *361*, 79–87.

Doyen, P. M. (1988), Permeability, conductivity, and pore geometry of sandstone, *J. Geophys. Res.*, *93*(B7), 7729–7740, doi:10.1029/JB093iB07p07729.

Draper, N. R., and H. Smith (2014), *Applied Regression Analysis*, John Wiley, Hoboken, N. J.

Ferréol, B., and D. H. Rothman (1995), Lattice-Boltzmann simulations of flow through Fontainebleau sandstone, in *Multiphase Flow in Porous Media*, edited by P. M. Adler, pp. 3–20, Springer, Netherlands.

Folk, R. L., and W. C. Ward (1957), Brazos river bar: A study in the significance of grain size parameters, *J. Sediment. Petrol.*, *27*(1), 3–26.

Fredrich, J. T., K. H. Greaves, and J. W. Martin (1993), Pore geometry and transport properties of Fontainebleau sandstone, *Int. J. Rock Mech. Min. Sci.*, *30*(7), 691–697, doi:10.1016/0148-9062(93)90007-Z.

Hayes, J. B. (1979), Sandstone Diagenesis—The Hole Truth, *Soc. Econ. Paleontol. Mineral., Spec. Publ.*, *26*, 127–139.

Hazlett, R. D. (1995), Simulation of capillary-dominated displacements in microtomographic images of reservoir rocks, *Transp. Porous Media*, *20*(1-2), 21–35, doi:10.1007/BF00616924.

Jackson, J. E. (2005), *A User's Guide to Principal Components*, John Wiley, Hoboken, N. J.

Jennings, B. R., and K. Parslow (1988), Particle size measurement: the equivalent spherical diameter, *Proc. R. Soc. A*, *419*(1856), 137–149, doi:10.1098/rspa.1988.0100.

Jolliffe, I. (2014), Principal component analysis, in *Wiley StatsRef: Statistics Reference Online*, John Wiley, Hoboken, N. J.

Katz, A. J., and A. H. Thompson (1986), Quantitative prediction of permeability in porous rock, *Am. Phys. Soc.*, *34*(11), 8179–8181.

Kløv, T., P. E. Øren, J. Å. Stensen, T. R. Lerdahl, L. I. Berge, S. Bakke, T. Boassen, and G. Virnovsky (2003), Pore-to-Field Scale Modeling of WAG, in *SPE Annual Technical Conference and Exhibition*, Society of Petroleum Engineers, Denver, Colo.

Krumbein, W. C. (1934), Size frequency distributions of sediments, *J. Sediment. Res.*, *4*(2), 65–77, doi:10.1306/D4268EB9-2B26-11D7-8648000102C1865D.

Krumbein, W. C., and G. D. Monk (1943), Permeability as a function of the size parameters of unconsolidated sand, *Trans. AIME*, *151*(1), 153–163, doi:10.2118/943153-G.

Latham, S., T. Varslot, and A. Sheppard (2008a), Automated registration for augmenting micro-CT 3D images, in *Proceedings of the 14th Biennial Computational Techniques and Applications and Applications Conference*, Australia and New Zealand Industrial and Applied Mathematics (ANZIAM), Canberra, Aus.

Latham, S., T. Varslot, A. Sheppard, and others (2008b), Image registration: Enhancing and calibrating X-ray micro-CT imaging, in *International Symposium of the Society of Core Analysts*, Abu Dhabi, UAE.

Marquardt, D. W. (1980), A critique of some ridge regression methods: Comment, *J. Am. Stat. Assoc.*, *75*(369), 87–91, doi:10.2307/2287388.

Martin, K. R. (1977), *Sedimentology of the Precipice Sandstone*, Univ. of Queensland, Surat Basin.

Martys, N. S., J. G. Hagedorn, D. Goujon, and J. E. Devaney (1999), Large-scale simulations of single- and multicomponent flow in porous media, vol. 3772, in Proceedings of the SPIE - International Society for Optical Engineering, pp. 205–213, Denver, Colo.

Mecke, K. R. (1996), Morphological characterization of patterns in reaction-diffusion systems, *Phys. Rev. E*, *53*(5), 4794–4800.

Metz, M., M. G. Briceño, E. Diaz, Q. Fang, A. Grader, and J. Dvorkin (2009), Properties of Tight Gas Sand From Digital Images, in *2009 Society of Exploration Geophysicists Annual Meeting*, Society of Exploration Geophysicists, Houston, Tex.

Pape, H., C. Clauser, and J. Iffland (1999), Permeability prediction based on fractal pore-space geometry, *Geophysics*, *64*(5), 1447–1460, doi:10.1190/1.1444649.

Paterson, M. S. (1983), The equivalent channel model for permeability and resistivity in fluid-saturated rock: A re-appraisal, *Mech. Mater.*, *2*(4), 345–352, doi:10.1016/0167-6636(83)90025-X.

Peng, S., F. Marone, and S. Dultz (2014), Resolution effect in X-ray microcomputed tomography imaging and small pore's contribution to permeability for a Berea sandstone, *J. Hydrol.*, *510*, 403–411, doi:10.1016/j.jhydrol.2013.12.028.

Riepe, L., M. H. Suhaimi, M. Kumar, and M. A. Knackstedt (2011), Application of High Resolution Micro-CT-Imaging and Pore Network Modeling (PNM) for the Petrophysical Characterization of Tight Gas Reservoirs: A Case History from a Deep Clastic Tight Gas Reservoir in Oman, in *SPE Middle East Unconventional Gas Conference and Exhibition*, Society of Petroleum Engineers, Muscat, Oman.

Sakellariou, A., T. J. Sawkins, T. J. Senden, and A. Limaye (2004), X-ray tomography for mesoscale physics applications, *Physica A*, *339*(1–2), 152–158, doi:10.1016/j.physa.2004.03.055.

Schladitz, K., J. Ohser, and W. Nagel (2006), Measuring intrinsic volumes in digital 3-D images, in *Discrete Geometry for Computer Imagery*, edited by A. Kuba, L. G. Nyúl, and K. Palágyi, pp. 247–258, Springer, Berlin.

Sheppard, A. et al. (2014), Techniques in helical scanning, dynamic imaging and image segmentation for improved quantitative analysis with X-ray micro-CT, *Nucl. Instrum. Methods Phys. Res. Sect. B*, *324*, 49–56, doi:10.1016/j.nimb.2013.08.072.

Sheppard, A. P., R. M. Sok, and H. Averdunk (2004), Techniques for image enhancement and segmentation of tomographic images of porous materials, *Physica A*, *339*(1–2), 145–151, doi:10.1016/j.physa.2004.03.057.

Sheppard, A. P., R. M. Sok, H. Averdunk, V. B. Robins, and A. Ghous (2006), Analysis of rock microstructure using high-resolution x-ray tomography, in *The International Symposium of the Society of Core Analysts*, Trondheim, Norway.

Sok, R. M., T. Varslot, A. Ghous, S. Latham, A. P. Sheppard, and M. A. Knackstedt (2009), Pore Scale Characterisation of Carbonates at Multiple Scales: Integration of Micro-CT, BSEM, and FIBSEM, in *International Symposium of the Society of Core Analysts,* Netherlands.

Swanson, B. F. (1981), A simple correlation between permeabilities and mercury capillary pressures, *J. Pet. Technol.*, *33*(12), 2498–2504, doi:10.2118/8234-PA.

Thompson, K. E., C. S. Willson, C. D. White, S. Nyman, J. Bhattacharya, and A. H. Reed (2005), Application of a New Grain-Based Reconstruction Algorithm to Microtomography Images for Quantitative Characterization and Flow Modeling, in *SPE Annual Technical Conference and Exhibition, Society of Petroleum Engineers*, Dallas, Tex.

Turner, M. L., L. Knüfing, C. H. Arns, A. Sakellariou, T. J. Senden, A. P. Sheppard, R. M. Sok, A. Limaye, W. V. Pinczewski, and M. A. Knackstedt (2004), Three-dimensional imaging of multiphase flow in porous media, *Physica A*, *339*(1–2), 166–172, doi:10.1016/j.physa.2004.03.059.

Van Baaren, J. P. (1979), Quick-look permeability estimates using sidewall samples and porosity logs, vol. 19, pp. 26–27, *Society of Professional Well Log Analysts*, London, U. K.

Varslot, T., A. Kingston, A. Sheppard, and A. Sakellariou (2010), Fast high-resolution micro-CT with exact reconstruction methods, vol. 7804, Proceedings of the SPIE - Progress in Biomedical Optics and Imaging, vol. 7804, Article number 780413.

Walsh, J. B., and W. F. Brace (1984), The effect of pressure on porosity and the transport properties of rock, *J. Geophys. Res.*, *89*(B11), 9425–9431, doi:10.1029/JB089iB11p09425.

Zhang, D., R. Zhang, S. Chen, and W. E. Soll (2000), Pore scale study of flow in porous media: Scale dependency, REV, and statistical REV, *Geophys. Res. Lett.*, *27*(8), 1195–1198, doi:10.1029/1999GL011101.

Zhang, X., and M. A. Knackstedt (1995), Direct simulation of electrical and hydraulic tortuosity in porous solids, *Geophys. Res. Lett.*, *22*(17), 2333–2336, doi:10.1029/95GL02230.